Check for updates

Europe
European Chemical
Societies Publishing

# Investigating the electrowetting of silver-based gas-diffusion electrodes during oxygen reduction reaction with electrochemical and optical methods

**Fabian Bienen**[1,2] ⬤ | **Melanie C. Paulisch**[3] | **Thorben Mager**[4] | **Jens Osiewacz**[5] | **Manigah Nazari**[1] | **Markus Osenberg**[6] | **Barbara Ellendorff**[5] | **Thomas Turek**[5] | **Ulrich Nieken**[4] | **Ingo Manke**[3] | **K. Andreas Friedrich**[1,2]

[1]Department Electrochemical Energy Technology, Institute of Engineering Thermodynamics, German Aerospace Center, Stuttgart, Germany

[2]Institute of Building EnergeticsThermal Engineering and Energy Storage, University of Stuttgart, Stuttgart, Germany

[3]Institute of Applied Materials, Helmholtz-Zentrum Berlin, Berlin, Germany

[4]Institute of Chemical Process Engineering, University of Stuttgart, Stuttgart, Germany

[5]Institute of Chemical and Electrochemical Process Engineering, Clausthal University of Technology, Clausthal-Zellerfeld, Germany

[6]Institute of Materials Science and Technology, Technical University Berlin, Berlin, Germany

**Correspondence**
Fabian Bienen, Institute of Engineering Thermodynamics, German Aerospace Center, Pfaffenwaldring 38–40, 70569 Stuttgart, Germany.
Email: fabianbienen@gmx.de
Melanie C. Paulisch, Institute of Applied Materials, Helmholtz-Zentrum Berlin, Hahn-Meitner-Platz 1, 14109 Berlin, Germany.
Email:
Melanie.Paulisch@helmholtz-berlin.de

**Abstract**

Porous gas-diffusion electrodes (GDEs) are widely used in electrochemical applications where a gaseous reactant is converted to a target product. Important applications for silver-based GDEs are the chlor-alkali and the $CO_2$ electrolysis processes in which silver catalyzes the oxygen- or carbon dioxide reduction reaction. The wetting of the porous GDEs is of utmost importance for the achieved performance of the electrode: a completely dry electrode will result in low current densities due to the reduced active surface area while on the other hand, a completely flooded electrode will deteriorate the access of the gaseous reactant. Therefore, we investigated silver-based GDEs for the oxygen reduction reaction with different amounts of the hydrophobic agent polytetrafluoroethylene (PTFE) and analyzed the potential-induced wetting behavior (electrowetting). The electrolyte breakthrough was recorded by a digital microscope and subsequently evaluated via imaging analysis of the observed breached electrolyte droplets. In order to characterize the wetting state during transition to the steady-state, we applied electrochemical impedance spectroscopy measurements and retrieved the double-layer capacitance. Our results indicate that a higher overvoltage facilitates the breakthrough of electrolytes through the gas-diffusion electrode. Surprisingly, a faster breakthrough of electrolyte was observed for electrodes with

2 of 12 **Electrochemical Science Advances**

RESEARCH ARTICLE
doi.org/10.1002/elsa.202100158

Chemistry
Europe
European Chemical
Societies Publishing

higher PTFE content. Porometry measurements revealed that the GDE with low PTFE content has a monomodal pore size distribution, whereas electrodes with higher PTFE amount exhibit a bimodal pore size distribution. In GDEs with monomodal pore size distribution the time in which the double layer capacitance is leveling off correlates with the breakthrough time of the electrolyte. In summary, we emphasize that the wetting of GDEs is a complex interplay of the applied potential, electrode composition, and resulting porous structure which requires further advanced measurements and analysis considering the parameters affecting the wetting behavior as a whole.

**KEYWORDS**

electrocapillarity, electrochemical impedance spectroscopy, electrowetting, gas-diffusion electrode, imaging analysis, oxygen reduction reaction (ORR), porous media

## 1 | INTRODUCTION

Gas-diffusion electrodes (GDEs) are used in several processes, like alkaline fuel cells,[1] metal-air batteries,[2] HCl,[3] $CO_2$,[4] or chlor-alkali[5] electrolysis. In these porous electrodes, a liquid or solid electrolyte is brought in contact with a gas phase and a solid electrocatalyst. Electrochemical conversion is assumed to take place in the close vicinity of the triple-phase boundary. Its shape and extension are crucial for the overall process performance because in this area the favored electrochemical reaction is taking place, for example, $O_2$ or $CO_2$ reduction. The electrode must ensure both, the intimate contact of the phases and also fast transport of educts and products to and from the reaction zone.

Silver-based GDEs have attained special attention for their use as the oxygen-depolarized cathode for chlor-alkali electrolysis. For this process, with a worldwide energy demand of at least 195.8 TWh in 2017,[6] a shift to this technology offers significant energy savings compared to the commonly used hydrogen-evolving cathodes Changing the cathode reaction to oxygen reduction (instead of hydrogen) reduces the cell potential by about 1 V at industrially relevant current densities, lowering the electrical energy demand around 30%.[5] The electrode consists of silver as catalyst phase, polytetrafluoroethylene (PTFE) acting as hydrophobic agent and binder, and a nickel mesh as current collector inside the GDE. The electrolyte distribution inside the GDE is determined by the electrode's wettability which is tuned in the manufacturing process by adding non-wetting additives like PTFE to prevent full flooding of the silver electrode. As shown by Franzen et al.,[7] there is a strong dependence of the porous structure on the PTFE content, which strongly influences the wettability and thus the overall electrochemical electrode

performance. It was shown, that higher PTFE contents lead to deposition of PTFE onto the pore walls, while the silver grains form a scaffold that is predominantly not affected. Therefore, the free pore space decreases leading to a significantly higher hydrophobic wall fraction in relation to the volume fraction. An optimum of about 2 wt% PTFE was determined in this study.

Another important phenomenon affecting the wettability of such an electrode is the so-called electrowetting or electrocapillary effect. In most cases, this effect is seen as a side-effect of electrode polarization under working conditions. De Mot et al.[8] showed the increase of perspiration for a carbon paper-based tin-PTFE-GDE in a $CO_2$ flow-by electrolyzer when changing the applied current density from 0 to 100 mA/cm$^2$ for differential pressures up to 80 mbar.[8] Song et al.[9] noticed that at high current densities of 400 mA/cm$^2$ B-doped copper-tin-GDEs stop working properly due to excessive penetration of the electrolyte through the GDE. Burchardt et al.[10] explained the drop of current density in PTFE-Pt-carbon GDEs with the enhanced flooding due to electrowetting. Lundblad and Björnbom[11] noticed the effect of electrode polarization on the wetting-in rate of the tested electrodes, which they further investigated in systematic research on that effect. They studied the initial wetting-in process of PTFE-bonded carbon electrodes.[12] Experiments were done in a half-cell immersed into 5.75 M potassium-hydroxide solution in potentiostatic or galvanostatic operation mode and variation of the oxygen partial pressure. The penetration depth and wetting-in rate after a certain time are strongly dependent on the applied potential, but only weakly on the applied current density. They concluded that the high current densities were promoting the entry of electrolyte only in initially wetted areas of the electrode but not to new, still unwetted regions. This work shows

that the electrowetting effect was dominant in their pore system, while other effects that strongly depend on the applied current density are of minor importance for the imbibition into new pores. These other effects might be the electroosmotic drag of water due to migration of hydroxide-ions and potassium-ions into the reaction zone or the volume increase due to adsorption of water from the gas phase at the locally high concentrated electrolyte.

However, to the best of our knowledge and according to Kubannek et al.[13] no particular attention was given to the electrowetting effect and so far, not much systematic research on the effect of electrowetting has been done for silver-PTFE-based GDEs. The only known works concerning electrowetting effects at silver GDEs are from Paulisch et al.[14,15] In Paulisch et al.[14] silver- GDEs with different PTFE content were investigated via operando X-ray-imaging techniques. It was shown that the degree of saturation, imbibition velocity as well as droplet formation at the backside of the GDE highly depend on the applied overpotentials. In Paulisch et al.[15] the electrolyte distribution within a GDE was analyzed via operando chronoamperometric measurements at a synchrotron facility. It was revealed that the electrolyte distribution inside the GDEs is fluctuating with increasing frequency at higher overpotentials. From these works it can be seen, that for a better understanding of the processes in the silver GDEs and their further performance improvement, a deeper understanding of the effects related to electrowetting is necessary.

## 1.1 | Electrowetting

Even if the phenomenon of electrowetting is known since Lippmann's first experiments in the 1870s[16] it recently received growing attention.[17] The attributed research focussed mainly on electrowetting on dielectric (EWOD) where a dielectric insulator with thicknesses on the nanometre and micrometer scale (depending on the applied potential and the insulator material e.g. a fluoropolymer like PTFE) is fixed on the surface of an electrode.

With the actuation of droplets, several applications can be created by moving, splitting, dosing, or merging droplets in microfluidic, artificial applications. This kind of application can be used to create microfluidic valves,[18] pumps[18] for lab-on-a-chip applications,[19] energy harvesting[20] or even to manipulate the optical behavior due to control of meniscus curvature.[21]

Less attention had been paid to the "classical" form of electrowetting where bare metal is in contact with an electrolyte solution. The major difference to EWOD is the limitation to lower applied voltages (due to possible electrolysis) and the dominant influence of the surface charge at the solid-electrolyte interface. As shown in Figure 1 the contact angle of a droplet of conducting liquid-like sodium hydroxide on the surface of the electrode will vary with the applied potential of the electrode.

As described in detail in the publications of Mugele et al.[17,22] the physical effect of electrowetting can be understood by the means of electrostatics, where electric fringe fields near the triple point area pull the electrolyte onto the electrode. For systems, where the corresponding length scale, the pore radius, is sufficiently larger than the screening length of the electrolyte or the dielectric length scale, this force can be reduced to a macroscopic additional stress at the triple point. This leads to a macroscopic change of the contact angle as can be seen from Figure 1.

A commonly used description of the contact angle change is the Young-Lippmann equation[22]

$$\cos(\Theta) = \cos(\Theta_0) + \eta \tag{1}$$

with

$$\eta = \frac{C_i \left(U_{pzc} - U\right)^2}{2\gamma_{lg}} \tag{2}$$

which expresses the change of the contact angle from an uncharged surface $\Theta_0$ (i.e. at the potential of zero charge) to the apparent contact angle $\Theta$ under an applied potential. The electrowetting number $\eta$ relates the electrostatic energy to the surface energy. The capacitance per unit area $C_i$ is a composition of the capacitance of the -if present-dielectric PTFE layer and the ion distribution in the liquid electrolyte. For the simplest cases of dilute solutions or thick insulating layers, analytical expressions for $C_i$ can be derived by the perfect conductor approximation or by the Poisson-Boltzmann (PB) equation (for different examples see the appendix of Mugele et al.[22]).

PTFE is a dielectric, insulating material: With the simplest assumption, the differential double-layer capacitance scales inverse linear with the dielectric layer thickness.[17] Due to the thickness of the dielectric PTFE layers inside the GDE a change of the contact angle only seems to be only realizable on the silver surface. Experimental works from Berry et al.[23] on thin fluoropolymer films are in accordance with this assumption.

However, for high concentrations, as used in our model system, 10 M NaOH-solution, a mean-field approximation like the PB equation is no longer sufficient. Recent publications have tried to overcome this issue by steric modifications[24] and the introduction of dipole ionic interactions.[25] However, these models still need some parametrization and do not include all effects related to a real porous system (e.g. surface roughness, chemical
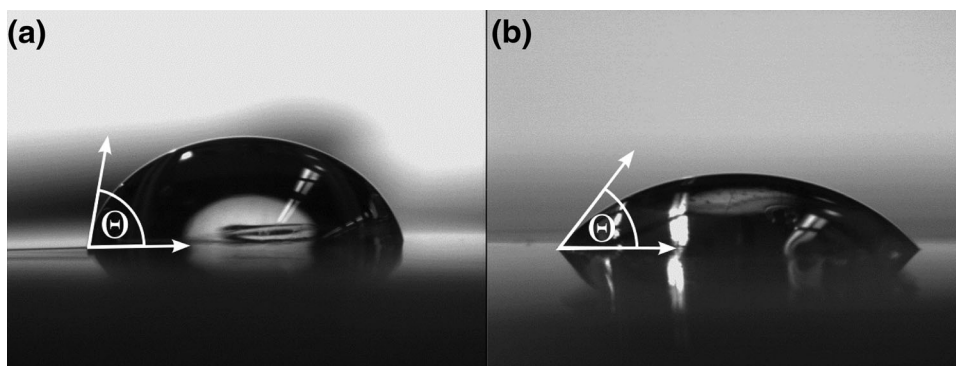
**FIGURE 1**    Visual effect of the contact angle change due to electrowetting for a 10 M NaOH solution on a mechanically polished silver plate. Counter (Pt) and reference electrode (Hg/HgO) are connected via a small hole in the 99.9% silver plate (not shown). a) Without applied potential, the averaged measured contact angle is 79.6° ± 4.3°, b) at an applied potential of 1 V vs. reversible hydrogen electrode, the contact angle reduces to 54.0° ± 3.4°

heterogeneity, and formation of oxide layers), which illustrates the need for experimental studies on such systems.

Certain ambiguities arise from the non-ideal (e.g. defects and aging) PTFE layers. Long-term operation of silver/PTFE GDEs in alkaline solution showed a partial decomposition of the PTFE component as reported by Wagner et al.[26] Additionally, as it can be seen from a time series of contact angle measurements on PTFE treated with an alkaline solution, the PTFE is going to be slightly more hydrophilic due to the chemical interaction with the electrolyte.[27] These effects seem to be neglectable for our model system for the first instance due to much shorter times of operation.

In this work, the potential induced wetting of silver-based GDEs with different PTFE contents is investigated to contribute to the understanding of the electrowetting effect of this type of GDEs during the oxygen reduction reaction (ORR). Therefore, the wetting state of the GDE was monitored operando via electrochemical impedance spectroscopy (EIS) and correlated with the breakthrough of the electrolyte through the GDE. Machine learning-supported imaging analysis of the resulting droplets was used to determine the breakthrough time and the droplet growth process.

## 2 | EXPERIMENTAL PROCEDURE

### 2.1 | Electrode preparation

GDEs were prepared according to the wet spraying method first described by Moussallem.[28] For each electrode, a suspension is prepared to contain 30 g silver particles (SF9ED, Ames Goldsmith Corporation, 99.99%) and PTFE dispersion (TF5060GZ, 3 M Dyneon) according to the desired PTFE content of the GDE. Additionally,

50 g of 1 wt% hydroxyethyl-methyl cellulose solution (WALOCEL MKX 70000 PP 01) in demineralized water is added.

For the electrode with high PTFE content, 40.0 g demineralized water is added to adjust the viscosity of the suspension. 80 layers of this suspension are sprayed onto a nickel mesh (106 × 118 $\mu m^2$ mesh size, 63 $\mu m$ thickness, Haver and Boecker OHG) with a hand spraying pistol (Evolution, 0.6 mm pinhole, Harder and Steenbeck). The Ni mesh stabilizes the Ag GDE mechanically and acts as a current collector. During spraying, the electrode is fixed on a heating table to realize a simultaneous drying, resulting in a homogeneous electrode surface. In the following steps, the electrode is hot pressed at 130°C and 15 MPa (Labo-Press P200S, Vogt, referenced to electrode area), and then sintered at 330°C for 15 min in an air furnace to burn out the methylcellulose and improve the mechanical stability. Electrodes with different PTFE contents, 3 wt% PTFE and 6 wt% PTFE were prepared using this method and will be in the following referred to as Ag97 and Ag94.

### 2.2 | Physical characterization

The thickness of the electrodes is determined after sintering by averaging measurements at six points using a thickness dial gauge (FD 50, Käfer GmbH). The pore size distribution of the electrodes is determined using a capillary-flow porometer. First wetting fluid (Porofil, Quantachrome) is applied on top of the electrode. Then the fluid is driven out of the electrode's pores by applying a nitrogen pressure gradient inside a capillary-flow porometer (Porometer 3G, Quantachrome), measuring the nitrogen flow through the pores. By comparing the nitrogen flow through wet and dry pores, a pore size distribution can be calculated.
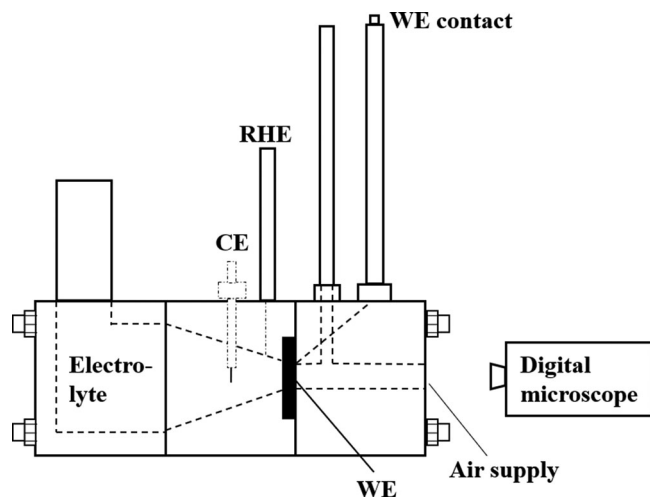
**FIGURE 2** Measurement setup including the Pt counter electrode (CE), reversible hydrogen electrode (RHE) as reference electrode, silver gas-diffusion electrode (GDE) as working electrode (WE). 30 wt% aqueous NaOH was used as an electrolyte. The backside of the GDE was filmed with a digital microscope to analyze percolating electrolyte droplets

Scanning electron microscopy (SEM) and focused ion beam (FIB) technology were applied to analyze the microstructure of the GDEs at high resolution. A piece of 5 mm x 5 mm was cut out from the centre of the electrode and horizontally mounted on a sample holder using a carbon pad. The coarse cuts were performed by applying an acceleration voltage of 30 keV and a current of 30 nA. The fine cuts were done at 30 keV and 7 nA. Images were taken at 1 keV and a pixel size of 20 nm. The analyses were performed at a Zeiss Crossbeam 340 Gallium-FIB/SEM.

## 2.3 | Breakthrough measurements

The breakthrough measurements were conducted in a three-electrode setup as shown in Figure 2 (more pictures can be found in the SI, Figure S1). Therefore, the silver GDE was used as working electrode ($A_{geom.}$ = 1 cm[2]), platinum foil (99.95%) as a counter electrode, and a reversible hydrogen electrode (RHE, Gaskatel) acted as reference electrode. Aqueous sodium hydroxide (30 wt%, VWR Chemicals) at room temperature (∼20°C) was used as electrolyte. For each experiment the same amount of fresh electrolyte was used so that the hydrostatic pressure (affects GDE wetting) was the same in all experiments. A hole in the backside of the electrochemical cell allows oxygen to enter while at the same time the backside of the GDE was filmed with a digital microscope (Toolkraft: Digimicro 2.0 scale, Resolution: 1920 × 1080, 19 frames per second) to determine the electrolyte's breakthrough time and characterize the droplet coverage of the GDEs backside.

The movies were converted into tiff images. Using the ImageJ software package Fiji,[29] images were grouped, and a median filter was applied over time to calculate one image for every second of the movie. This procedure offers the advantages to improve the signal-to-noise ratio by decreasing the noise and reducing the data volume. The formation of the droplets was reconstructed using the pixel classification approach of the software package ilastik.[30] After the segmentation the droplets were separated by using a three-dimensional distance transform watershed method via the MorpholibJ[31] plugin and measured by the particle analyzing method of Fiji.[29]

The EIS spectra were recorded in potentiostatic operation mode (200 and 500 mV) with a ZAHNER-Elektrik GmbH & Co. KG Zennium electrochemical workstation. The spectra were recorded in a frequency range of 500 MHz–300 kHz with an excitation voltage of 20 mV for all experiments. Each experiment was at least conducted twice. To monitor the time-dependent wetting of the GDE the spectra were recorded consecutively with a time resolution of 3 min for the experiments at 200 mV and 4 min for the experiments at 500 mV. Subsequently, the evaluation of the spectra was performed with the RelaxIS 3 software (RHD instruments GmbH & Co. KG). Each spectrum was fitted to an equivalent circuit model (EQCM) to extract the admittance of the R-CPE (constant-phase element) attributed to the charge transfer. These values were used to calculate the effective interfacial differential double layer capacitance $C_{dl}$ via Brug's equation (3) in which $R_{ct}$ is the charge transfer resistance, $R_{\Omega}$ the ohmic resistance, and $Q$ and $\alpha$ represent the admittance and exponent of a CPE.[32] $C_{dl}$ serves herein as an approximation for the electrochemical surface area (ECSA) which is proportional to the wetted surface area.

$$C_{dl} = Q^{\frac{1}{\alpha}} \left( \frac{R_{\Omega} R_{ct}}{R_{\Omega} + R_{ct}} \right)^{\frac{(1-\alpha)}{\alpha}} \qquad (3)$$

Further information about the general electrochemical performance of the silver-based GDEs can be found in the contribution of Franzen et al.[7]

## 3 | RESULTS AND DISCUSSION

### 3.1 | Physical characterization

The thickness measurement of the electrodes showed an average thickness of 280 ± 18 μm for Ag97 and 296 ± 5 μm for Ag94. Figure 3 shows the microstructure of the GDEs with different chemical compositions. Both GDEs show twinned silver grains (silver grains marked with blue arrows, twins with red arrows) which form a framework.
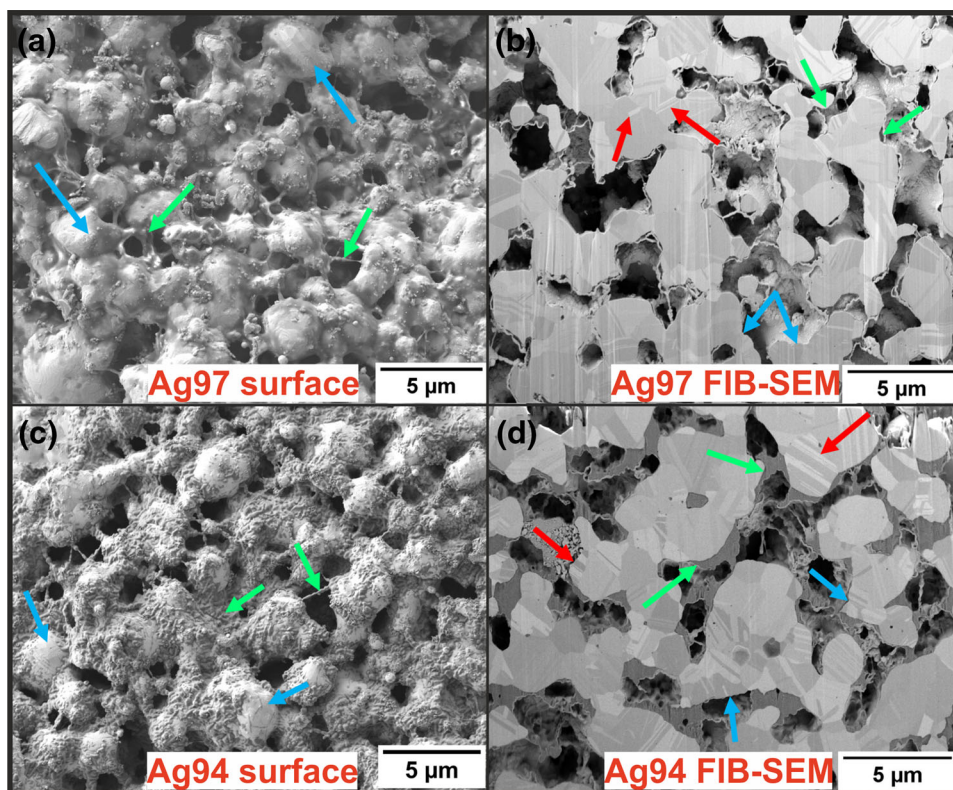
**FIGURE 3**    Focused ion beam/scanning electron microscopy (FIB/SEM), microstructure of silver-based gas-diffusion electrodes (GDEs), silver grains (blue arrows), twins (red arrows), polytetrafluoroethylene (PTFE) (green arrows), and pore network (dark grey/black). (a) Ag97 surface, (b) cutting surface Ag97, (c) Ag94 surface, and (d) Ag94 cutting surface

The PTFE (green arrows) is located at the silver grains while in general, the microstructure reveals a complex open pore network. As shown by Franzen et al.[7] the PTFE areas at the silver grains become larger with increasing PTFE content while the form and size of the silver framework are hardly influenced. Thus, the pore volume and the pore size decrease. Therefore, Ag97 shows larger pores than Ag94.

The porometry measurements (cf. Figure 4) reveal two important findings: Firstly, the void pore space of the GDE with higher PTFE content (Ag94) is significantly smaller compared to the GDE with lower PTFE content (Ag97). For Ag97 we determined a mass normalized pore volume of 1.761 $cm^3$ $g^{-1}$, for Ag94 only 0.735 $cm^3$ $g^{-1}$. Secondly, Ag97 shows a monomodal pore size distribution around ~810 nm while for Ag94 a bimodal distribution located at ~840 and ~540 nm can be observed.

## 3.2 | Extracting the double layer capacitance $C_{dl}$ from potentiostatic EIS

Based on a previous work of our group an exemplary evaluation of the potentiostatic EIS measurements for Ag97 at 200 mV is depicted in Figure 5.[33] The time-dependent raw
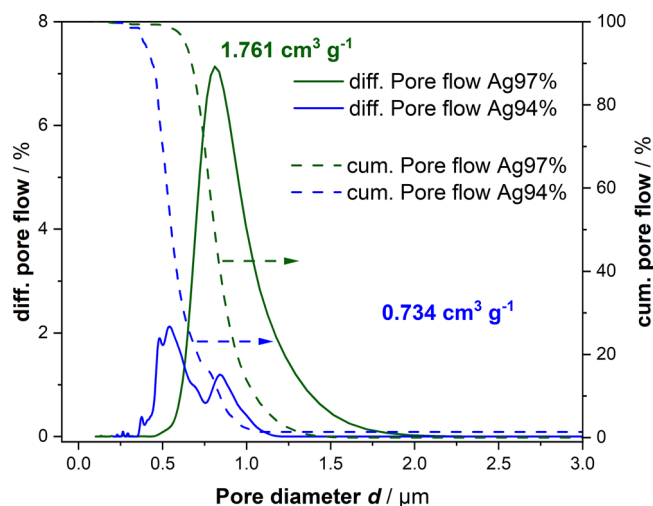


**FIGURE 4**    Porometry results reveal a monomodal pore size distribution for Ag97 and a bimodal distribution for Ag94. Furthermore, the void pore space of Ag97 is twice as high as for Ag94

data of the -Nyquist spectra (symbols) were fitted (lines) to an EQCM consisting of an inductor (cables), a resistance describing the ohmic losses and two R-CPE describing the ionic movement in the porous electrode and the charge
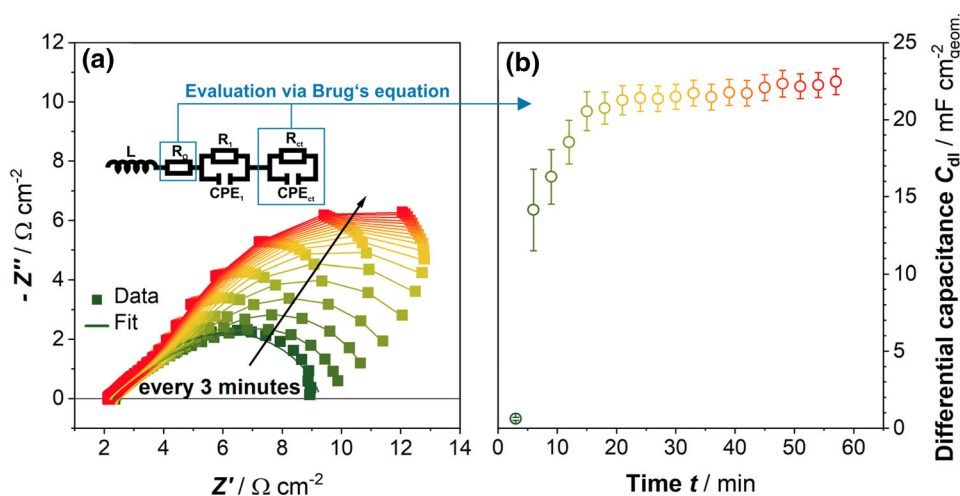
**FIGURE 5**  Evaluation routine for potentiostatic electrochemical impedance spectroscopy (EIS) measurements for Ag97 gas-diffusion electrode (GDE) at 200 mV. (a) Time course of the impedance spectra and used equivalent circuit for fitting and extracting $C_{dl}$ values, (b) Corresponding time course of the extracted $C_{dl}$ values

transfer. To estimate the ECSA via fitting extracted ohmic resistance, charge transfer resistance and corresponding CPE parameters were used to calculate the effective differential double layer capacitance $C_{dl}$ using Brug's correlation (cf. (3)).[32] The calculated time course of the $C_{dl}$ values, which is a measure of the wetting state of the GDE, is shown in Figure 5b) and demonstrates a sharp rise of the ECSA at the beginning of the experiment until a plateau is reached. The shape of the curve can be described by the Washburn equation (cf. (4)) which balances capillary and viscous forces and postulates that the penetration depth $l_{penetration}$ (determining the ECSA value) is proportional to the square root of both, the time $t$ and pore radius $r$ while the penetration velocity is directly proportional to $r$ and inverse proportional to the length which is already filled with electrolyte (cf. (5)).[34] The material and electrolyte properties: surface energy (affected by potential variation), dynamic viscosity, and contact angle are included in the capillary constant. However, the equation fails to describe the $C_{dl}$ course at the point where a plateau is reached since only an advancing front is accounted for. Nevertheless, equation (4) satisfactorily describes the time course of the $C_{dl}$ values (for EIS experiments at 200 mV) until it levels off. Therefore, the imbibition dynamics are suggested to be determined by capillary and viscous forces.

$$l_{penetration} = \sqrt{k_{capillary}} * \sqrt{r} * \sqrt{t} \quad (4)$$

$$\frac{dl_{penetration}}{dt} = \frac{1}{2} k_{capillary} * r * l_{penetration}^{-1} \quad (5)$$

## 3.3 | Influence of the GDEs PTFE content and applied potential on $C_{dl}$ and electrolyte breakthrough

### 3.3.1 | Imaging analysis

Figure 6a–c shows representative images of the droplet pattern (bright grey) which were formed during the tests for the Ag97 and Ag94 GDE at different applied potentials. As first step to characterize the droplet formation, the time of penetration was measured, which is indicated by the time when the first droplets form (cf. Figure 6d, pink arrows).

In general, the breakthrough time for Ag97 is higher than for Ag94 while droplets form later for lower potentials. The images are shown in Figure 6a,c were taken 25 min after the first droplets form for each respective measurement. In case of Ag97 at 500 mV, the image shows the situation 60 min after the first droplet was formed, due to the slower droplet growth (Figure 6d,f). For Ag97 (Figure 6a,b) a homogeneous distribution of fine droplets over the measured surface area is visible. In comparison to Figure 6a, the droplets in Figure 6b are smaller, which is indicating a faster droplet growth for higher overpotentials. Ag94 shows two classes of droplet sizes (Figure 6c). Paulisch et al.[15] observed by means of electrochemical operando synchrotron radiographies that pore paths which are filled with electrolyte stay filled while other paths remain free. This result is in good agreement with the observed droplet pattern in this work: Once a percolating pore path is formed by the electrolyte, a droplet forms and continuous electrolyte flow leads to droplet growth. Additionally, the recent measurements
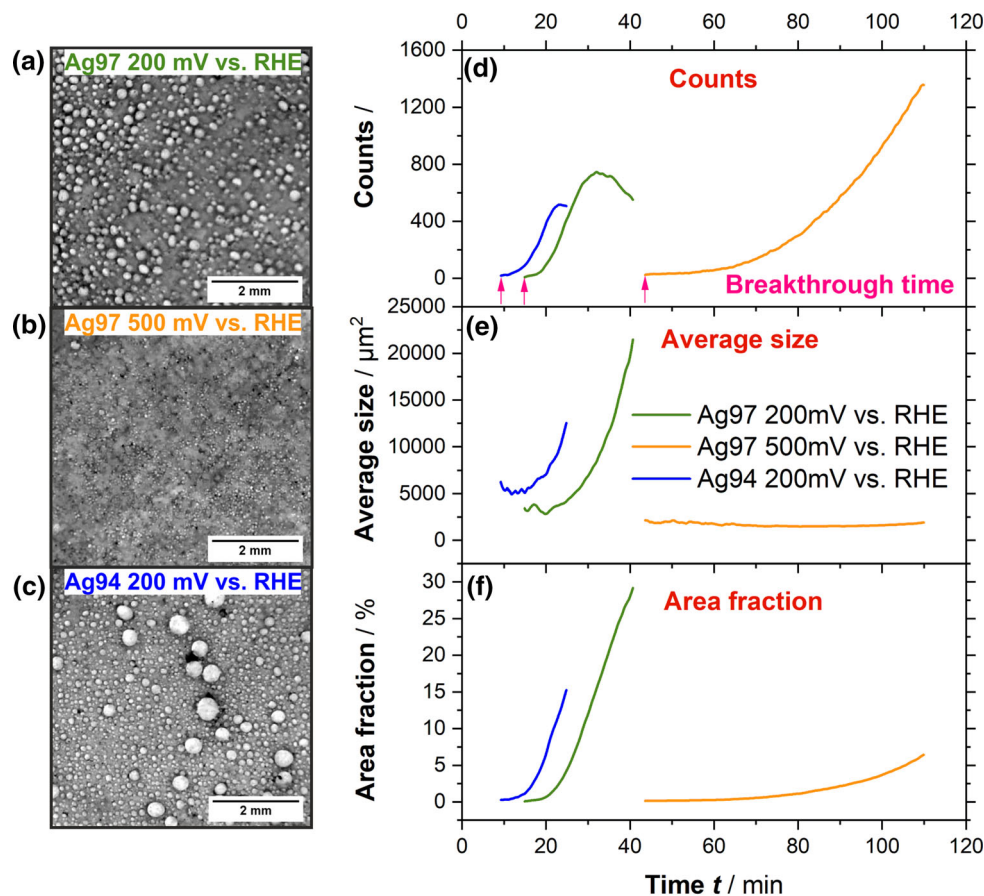
**FIGURE 6** (a) Droplet pattern (bright grey), Ag97 at 200 mV versus reversible hydrogen electrode (RHE), 25 min after first droplets form, (b) Ag97 at 500 mV versus RHE, 60 min after first droplets form, (c) Ag97 at 200 mV versus RHE, 25 min after first droplets form, d) number of droplets, e) average size of droplets, and f) area fraction of droplet covered surface

reveal the formation of homogenous droplet pattern in case of homogeneous microstructures.

For a detailed analysis of the droplet formation, the number, the average droplet size, and the droplet area fraction were calculated for both kinds of GDEs (Figure 6d–f).

Figure 6d shows the number of droplets over the time in dependence of the chemical composition of the GDE and the applied potential. At 200 mV both GDEs show a fast formation of a large number of droplets until the curves reach a maximum and the number of droplets is decreasing. For 500 mV the amount of the droplets increases slowly in the beginning of the percolation process. We supposed that these processes follow the same curve characteristics as described for the processes at 200 mV, thus a maximum is expected. However, due to the lower overpotential the process is decelerated and only the beginning of the curve can be seen for the measurement at 500 mV. Figure 6e shows the average surface size of the droplets. For 200 mV the droplets grow fast and continuously for both kinds of GDE while for 500 mV the droplets show a very slow growth. Figure 6f shows the percentage area fraction of the droplets and indicates how much

of the GDE surface is covered. At an applied potential of 200 mV, the fraction area of droplets is growing quite fast. For 500 mV, the droplet covering is much slower. In conclusion at 200 mV, many droplets form in a short time, which grow fast and continuously until a maximum of quantity is reached. While the amount is decreasing the average size and the area fraction is increasing continuously. This is a hint that small droplets agglomerate to large droplets during the growing process. At a lower potential of 500 mV the formation and grow processes are decelerated. Nevertheless, it is to be expected that they are following the same procedure. Furthermore, in case of Ag94 the formation and growth are faster than for Ag97.

As shown in Figure 6c, the droplets at the end of the measurements show two class sizes for Ag94. Therefore, histograms of the droplet sizes at 200 mV were plotted for different times for both GDEs (Figure 7).

For Ag97 a maximum form at 2000 $\mu m^2$ after 1200 s. The peak position remains at 2000 $\mu m^2$ for 900 s while the peak height increases. This demonstrates, that the number of droplets increases, however, no significant growth of the droplets takes place in this time period. After 2100
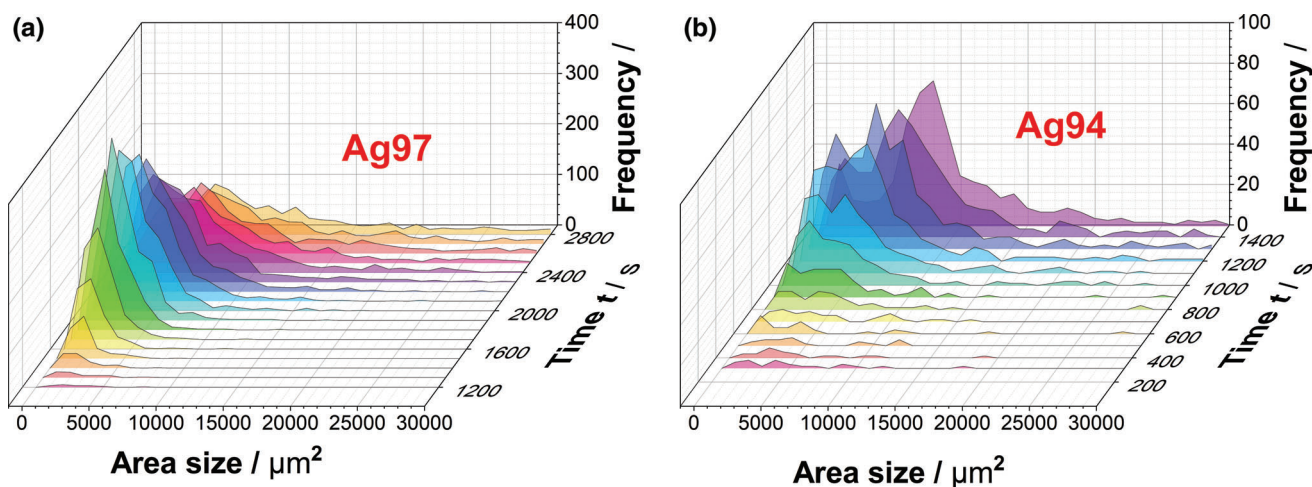
**FIGURE 7**      Histograms of the droplet sizes over time at 200 mV versus reversible hydrogen electrode (RHE), (a) Ag97, )b) Ag94

s the maximum moves slowly to higher class sizes, while the maximum is decreasing, indicating a smaller number of larger droplets. For Ag94 two small maxima at 1000–2000 $\mu m^2$ and 4000 $\mu m^2$ form after 300 s which can be explained by the, in contrast to Ag97, bimodal pore system (cf. Figure 4). In the following time both maxima grow but remain at these class sizes for additional 1000 s. After 1300 s, the second maximum increases and moves to higher class sizes, while the first maximum decreases and remains at 1000–2000 $\mu m^2$. This behavior indicates, that existing droplets grow, while continuously new small droplets appear.

### 3.3.2 | Electrochemical analysis

The potential-dependent time course of the $C_{dl}$ values for Ag97 is illustrated in Figure 8a. The corresponding time course of the resulting current is depicted in Figure S2. However, similar shapes of both $C_{dl}$ curves are observed: initially a sharp rise of $C_{dl}$ followed by a plateau. For both potentials the time of electrolyte breakthrough correlates with the times observed until the $C_{dl}$ plateaus are reached. Interestingly, the achieved plateaus are suggested not to be solely the result of equilibrated viscous and capillary forces but more likely representing the finite thickness of the GDE restricting further imbibition. Additionally, the coincidence of the breakthrough time and time period to reach the $C_{dl}$ plateau indicates that the electrolyte's imbibition into the Ag97 GDE is a uniform process. After the breakthrough of electrolyte, the $C_{dl}$ values stay almost constant. Thus, we suppose that the electrolyte imbibes homogeneously into the GDE. This uniform imbibition is likely due to the homogeneous pore size distribution (cf. Figure 4) as evidenced by a monomodal electrolyte droplet size at the beginning of the breakthrough over the

whole visible area. However, to rule out the impact of GDE thickness, the thickness normalized breakthrough time was calculated and reveals that the gap between the breakthrough times is significant. This faster breakthrough for the GDE operated at 200 mV can be explained by the potential dependence of the surface energy, respectively the contact angle for the solid-liquid interface. As postulated by Lippmann the solid-liquid surface energy is reduced whenever the potential is shifted further away from the potential of zero charge.[16] As already mentioned this phenomenon is commonly termed electrowetting. Furthermore, this observation is in good agreement with the analyses of Paulisch et al.[14], who demonstrated a faster saturation of the GDEs, faster droplet formation and higher electrolyte fluctuations for higher overpotentials. In accordance, a GDE operated at OCV for 36 h (averaged potential 1.125 V vs. RHE) did not show any electrolyte breakthrough emphasizing the necessity of electrode polarization to induce a wetting process.

A comparison of the $C_{dl}$ values and breakthrough times for Ag97 and Ag94 is depicted in Figure 8b. It can be observed that the breakthrough time for the GDE with a higher PTFE content is shorter compared to the GDE with less PTFE which seems to be counter intuitive since PTFE is usually used as hydrophobic agent. A reason for this unexpected behavior may be the difference in pore size distribution (cf. Figure 4). While Ag97 shows a narrow monomodal pore size distribution around ~810 nm Ag94 features two distinct peaks at ~840 and ~540 nm. This agrees with Franzen et al.[7] who showed that a higher amount of PTFE is decreasing the diameter of the pore throats due to the arrangement of larger PTFE areas at the silver grains. Fazeli et al.[35] analyzed proton exchange membrane fuel cell's gas diffusion layers and observed that capillary forces are the most important factor which enables water to enter the system. Therefore, we suppose
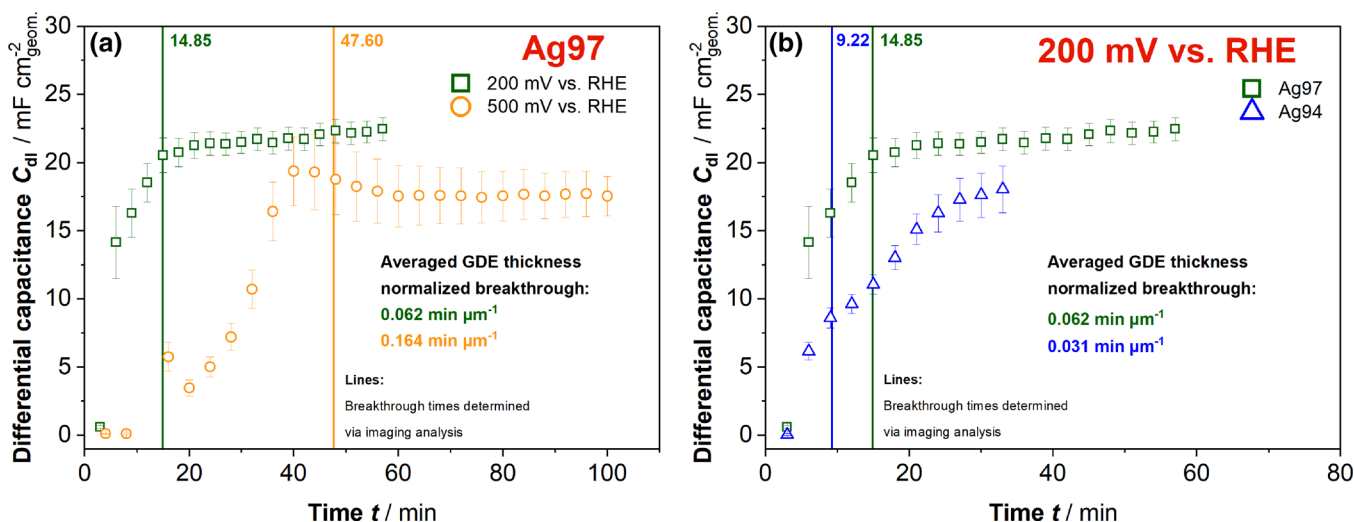
**FIGURE 8** (a) Potential dependent $C_{dl}$ values for the gas-diffusion electrode (GDE) with 97 w% Ag, 3 w% polytetrafluoroethylene (PTFE) and corresponding breakthrough time evaluated from imaging analysis, (b) Influence of the PTFE content onto the time course of the $C_{dl}$ values at 200 mV versus reversible hydrogen electrode (RHE)

that the increased capillary forces (proportional to $r^{-1}$, Young-Laplace equation) in smaller pores facilitate the imbibition velocity. Contradictorily, the Washburn equation which balances the capillary forces with the counter acting viscous forces (cf. (5)) predicts a straight proportionality of the imbibition velocity with the pore radius $r$. However, Washburn's model is a simplified model of a bundle of capillaries and does not consider the heterogeneity of the wetting behavior of the pore walls. Another possible explanation for the faster breakthrough for Ag94 might be that the aqueous electrolyte is 'slipping' over the hydrophobic PTFE regions since the electrolyte does not penetrate into the inherent surface roughness of PTFE while on the other hand the electrolyte will imbibe into the surface roughness of the hydrophilic silver grains[14] which will result in a slower penetration velocity. These two phenomena regarding the effect of surface structure onto the wetting behavior of surfaces were postulated by Cassie-Baxter[36] and Wenzel.[37] Furthermore, in contrast to Ag97 the breakthrough time of Ag94 does not correlate with the time necessary to reach the plateau of $C_{dl}$ (cf. Figure 6b) indicating an additional to Washburn's correlation occurring underlying effect during electrolyte imbibition. The $C_{dl}$ curve for Ag94 follows the $t^{0.5}$ proportionality suggesting that Washburn's equation is at least partially applicable to model the imbibition until a stationary state is achieved. We suspect that the discrepancy of the electrolyte breakthrough time and the time necessary to achieve the $C_{dl}$ plateau is evoked by the parallel existence of two pore size regimes which will result in different imbibition velocities.

However, as seen above the interpretation of potential induced imbibition experiments for GDEs is very challenging and requires more detailed analyses about the three-dimensional microstructure of the GDEs to build a clear picture of the microstructural influences on the electrolyte distribution. Furthermore, more analyses about the impact of electrowetting effects during the operation of GDEs at various temperatures as well as electrolyte and chemical compositions are needed.

Ultimately, the presented findings might be transferred to other systems in which porous electrodes e.g., based on deposited nanoparticles on carbon paper, are used to convert e.g., $CO_2$. The underlying phenomena influencing the electrolyte's penetration into the porous network (porous architecture, applied potential, electrolyte properties) can be expected to remain the same since they do not depend on the considered material system. In the special case of the conversion of $CO_2$, the precipitation of hydrophilic carbonate salts will also affect the electrode's wetting behavior.

## 4 | CONCLUSIONS

In this work, the potential-induced wetting of silver-based GDEs with different compositions (amount of hydrophobic agent PTFE) was investigated at different potentials during the ORR. The differential double layer capacitance $C_{dl}$ was determined via EIS and was found to resemble the wetting state of the GDE. Furthermore, imaging analysis of the droplet breakthrough was used to determine the breakthrough time. At OCV the electrolyte is not able to imbibe the highly hydrophobic GDE, while imbibition and breakthrough of electrolyte are observed at applied overpotentials. This can be explained by a surface energy reduction of the liquid-solid interface when applying

11 of 12 **Electrochemical Science Advances**

RESEARCH ARTICLE
doi.org/10.1002/elsa.202100158

Chemistry
Europe
European Chemical
Societies Publishing

potentials further away from the potential of zero charge (cf. (1)) as postulated by the Lippmann equation. Additionally, our results demonstrate that for a homogeneous pore system the extracted double-layer capacitance might be a good indicator to determine the wetting state of the GDE operando since the visually observed breakthrough time of electrolyte and the time when the $C_{dl}$ values achieve a plateau correlate. Once the breakthrough is observed, $C_{dl}$ values remain constant. Furthermore, the shape of the $C_{dl}$ curve follows the correlation of Washburn until a stationary state of wetting is achieved indicating that the wetting process is determined by capillary and viscous forces. Surprisingly, the GDE with a higher content of hydrophobic agent showed a faster electrolyte breakthrough. Whereas the GDE with a lower PTFE content has a monomodal pore size distribution ($\sim$810 nm), the GDE with an increased PTFE content has a bimodal pore size distribution ($\sim$840 nm, $\sim$540 nm). These monomodal and bimodal characteristics were also observed during the histogram analysis of the droplet sizes at the backside of the GDE: the electrode with a bimodal pore size distribution showed a bimodal droplet sizes distribution and analogously the same behavior was observed for the monomodal system. The existence of smaller pores inside the GDE with a higher PTFE amount might be one reason for a faster breakthrough of electrolytes due to the increased capillary forces. On the other hand, a smaller pore radius will lead to a decelerated imbibition velocity as predicted by Washburn's equation (cf. (5)). This challenging interpretation of the shown electrowetting experiments demonstrates that the potential induced electrolyte imbibition into a GDE is a complex interplay of the applied potential, electrode composition, and resulting pore architecture. Therefore, further investigations are necessary to create a better understanding of the wetting process of these heterogeneous systems.

## ACKNOWLEDGMENTS

## CONFLICT OF INTEREST

The authors declare no conflict of interest.

## ORCID

*Fabian Bienen* ![ORCID] https://orcid.org/0000-0002-4660-8826

## REFERENCES

1. T. B. Ferriday, P. H. Middleton, *Int. J. Hydrogen Energy* **2021**, *46*(35), 18489. https://doi.org/10.1016/j.ijhydene.2021.02.203.
2. C. Wang, Y. Yu, J. Niu, Y. Liu, D. Bridges, X. Liu, J. Pooran, Y. Zhang, A. Hu, *Appl. Sci.* **2019**, *9*(14), 2787. https://doi.org/10.3390/app9142787.
3. T. Vidakovic-Koch, I. Gonzalez Martinez, R. Kuwertz, U. Kunz, T. Turek, K. Sundmacher, *Membranes* **2012**, *2*(3), 510. https://doi.org/10.3390/membranes2030510.
4. T. Burdyny, W. A. Smith, *Energy Environ. Sci.* **2019**, *12*(5), 1442. https://doi.org/10.1039/c8ee03134g.
5. I. Moussallem, J. Jörissen, U. Kunz, S. Pinnow, T. Turek, *J. Appl. Electrochem.* **2008**, *38*(9), 1177. https://doi.org/10.1007/s10800-008-9556-9.
6. J. Kintrup, M. Millaruelo, V. Trieu, A. Bulan, E. S. Mojica, *Electrochem. Soc. Interf.* **2017**, *26*(2), 73. https://doi.org/10.1149/2.f07172if.
7. D. Franzen, B. Ellendorff, M. C. Paulisch, A. Hilger, M. Osenberg, I. Manke, T. Turek, *J. Appl. Electrochem.* **2019**, *49*(7), 705. https://doi.org/10.1007/s10800-019-01311-4.
8. B. de Mot, J. Hereijgers, M. Duarte, T. Breugelmans, *Chem. Eng. J.* **2019**, *378*, 122224. https://doi.org/10.1016/j.cej.2019.122224.
9. Y. Song, J. R. C. Junqueira, N. Sikdar, D. Ohl, S. Dieckhofer, T. Quast, S. Seisel, J. Masa, C. Andronescu, W. Schuhmann, *Angewandte Chemie Internation Edition* **2021**, *60*(16), 9135. https://doi.org/10.1002/anie.202016898.
10. T. Burchardt, *J. Power Sources* **2004**, *135*(1), 192. https://doi.org/10.1016/j.jpowsour.2004.03.072.
11. A. Lundblad, P. Bjornbom, *J. Electrochem. Soc.* **1992**, *139*(5), 1337. https://doi.org/10.1149/1.2069408.
12. A. Lundblad, P. Bjornbom, *J. Electrochem. Soc.* **1994**, *141*(6), 1503. https://doi.org/10.1149/1.2054953.
13. F. Kubannek, T. Turek, U. Krewer, *Chem. Ing. Tech.* **2019**, *91*(6), 720. https://doi.org/10.1002/cite.201800181.
14. M. C. Paulisch, M. Gebhard, D. Franzen, A. Hilger, M. Osenberg, N. Kardjilov, B. Ellendorff, T. Turek, C. Roth, I. Manke, *Materials* **2019**, *12*(17), 2686. https://doi.org/10.3390/ma12172686.
15. M. C. Paulisch, M. Gebhard, D. Franzen, A. Hilger, M. Osenberg, S. Marathe, C. Rau, B. Ellendorff, T. Turek, C. Roth, I. Manke, *ACS Appl. Energy Mater.* **2021**, *4*, 7497. https://doi.org/10.1021/acsaem.1c01524.
16. G. Lippmann, *Annales de Chimie et de Physique* **1875**, *5*, 494.
17. F. Mugele, J. - C. Baret, *J. Phys. Condens. Matter* **2005**, *17*(28), R705. https://doi.org/10.1088/0953-8984/17/28/R01.
18. J. Kedzierski, S. Berry, B. Abedian, *J. Microelectromech. Syst.* **2009**, *18*(4), 845. https://doi.org/10.1109/jmems.2009.2023845.
19. S. Haeberle, R. Zengerle, *Lab Chip* **2007**, *7*(9), 1094. https://doi.org/10.1039/b706364b.
20. T. Krupenkin, J. A. Taylor, *Nat. Commun.* **2011**, *2*, 448. https://doi.org/10.1038/ncomms1454.
21. L. Hou, J. Zhang, N. Smith, J. Yang, J. Heikenfeld, *J. Micromech. Microeng.* **2010**, *20*(1), 015044. https://doi.org/10.1088/0960-1317/20/1/015044.
22. F. Mugele, J. Buehrle, *J. Phys. Condens. Matter* **2007**, *19*(37), 375112. https://doi.org/10.1088/0953-8984/19/37/375112.
23. S. Berry, J. Kedzierski, B. Abedian, *J. Colloid Interface Sci.* **2006**, *303*(2), 517. https://doi.org/10.1016/j.jcis.2006.08.004.
24. I. Borukhov, D. Andelman, H. Orland, *Phys. Rev. Lett.* **1997**, *79*(3), 435. https://doi.org/10.1103/PhysRevLett.79.435.

12 of 12 **Electrochemical Science Advances**

RESEARCH ARTICLE
**doi.org/10.1002/elsa.202100158**

**Chemistry Europe**
European Chemical
Societies Publishing

25. R. M. Adar, T. Markovich, D. Andelman, *J. Chem. Phys.* **2017**, *146*(19), 194904. https://doi.org/10.1063/1.4982885.

26. N. Wagner, M. Schulze, E. Gülzow, *J. Power Sources* **2004**, *127*(1–2), 264. https://doi.org/10.1016/j.jpowsour.2003.09.022.

27. Y. Rotenberg, S. Srinivasan, E. I. Vargha-Butler, A. W. Neumann, *J. Electroanal. Chem. Interfacial Electrochem.* **1986**, *213*(1), 43–51. https://doi.org/10.1016/0022-0728(86)80596-4.

28. I. Moussallem, Development of Gas Diffusion Electrodes for a New Energy Saving Chlor-Alkali Electrolysis Process. Dissertation, Institute of Chemical Process Engineering, TU Clausthal, **2011**.

29. J. Schindelin, I. Arganda-Carreras, E. Frise, V. Kaynig, M. Longair, T. Pietzsch, S. Preibisch, C. Rueden, S. Saalfeld, B. Schmid, J. Y. Tinevez, D. J. White, V. Hartenstein, K. Eliceiri, P. Tomancak, A. F Cardona, *Nat. Methods* **2012**, *9*(7), 676. https://doi.org/10.1038/nmeth.2019.

30. S. Berg, D. Kutra, T. Kroeger, C. N. Straehle, B. X. Kausler, C. Haubold, M. Schiegg, J. Ales, T. Beier, M. Rudy, K. Eren, J. I. Cervantes, B. Xu, F. Beuttenmueller, A. Wolny, C. Zhang, U. Koethe, F. A. Hamprecht, A. Kreshuk, *Nat. Methods* **2019**, *16*(12), 1226. https://doi.org/10.1038/s41592-019-0582-9.

31. D. Legland, I. Arganda-Carreras, P. Andrey, *Bioinformatics* **2016**, *32*(22), btw413. https://doi.org/10.1093/bioinformatics/btw413.

32. G. J. Brug, A. L. G. van den Eeden, M. Sluyters-Rehbach, J. H. Sluyters, *J. Electroanal. Chem. Interfacial Electrochem.* **1984**, *176*(1), 275. https://doi.org/10.1016/S0022-0728(84)80324-1.

33. F. Bienen, A. Löwe, J. Hildebrand, S. Hertle, D. Schonvogel, D. Kopljar, N. Wagner, E. Klemm, K. A. Friedrich, *J. Energy Chem.* **2021**, *62*, 367. https://doi.org/10.1016/j.jechem.2021.03.050.

34. E. W. Washburn, *Phys. Rev.* **1921**, *17*, 273. https://doi.org/10.1103/PhysRev.17.273.

35. M. Fazeli, J. Hinebaugh, A. Bazylak, *J. Electrochem. Soc.* **2015**, *162*(7), F661. https://doi.org/10.1149/2.0191507jes.

36. A. B. D. Cassie, S. Baxter, *Trans. Faraday Soc.* **1944**, *40*, 546. https://doi.org/10.1039/TF9444000546.

37. R. N. Wenzel, *Ind. Eng. Chem.* **1936**, *28*(8), 988. https://doi.org/10.1021/ie50320a024.

## SUPPORTING INFORMATION

Additional supporting information may be found in the online version of the article at the publisher's website.